

## COB-2019-0368

# INVESTIGATION OF TURBULENT FLOWS OVER A NACA0012 AIRFOIL USING STATISTICAL POST-PROCESSING OF LARGE EDDY SIMULATIONS

**Gabriel B. Nogueira**

[gabrielbarrosnog@gmail.com](mailto:gabrielbarrosnog@gmail.com)

**William R. Wolf**

[wolf@fem.unicamp.br](mailto:wolf@fem.unicamp.br)

School of Mechanical Engineering, University of Campinas, 13083-860, Campinas - SP, Brazil

**Abstract.** The study of turbulent flows over airfoils finds application in aeronautical and wind energy research where drag and noise reduction are sought. In this work, we combine high-fidelity simulations with statistical post-processing tools to provide a better understanding of physical processes related to turbulent flows in the presence of walls with adverse pressure gradient variations. Wall resolving large eddy simulation is the method of choice to simulate the current flows. An investigation of the mechanisms of production, advection, transport and dissipation is provided through analysis of the turbulent kinetic energy (TKE) budgets and other turbulence statistics such as the Lumley triangle and Reynolds stress anisotropy tensor. Simulations are performed for different meshes in order to verify convergence of statistics. Moreover, different tripping configurations are analyzed to assess their impact on the present flows.

**Keywords:** Large eddy simulation, Turbulent flow, Aerodynamics, Anisotropy, Turbulent kinetic energy

### 1. INTRODUCTION

Studies of flows past airfoils find application in the design of aircraft wings, industrial rotors (Gourdain *et al.*, 2017), and wind and gas turbines for the production of energy (Li *et al.*, 2015; Oerlemans, 2009). More recently, airfoil flows have also been studied for the design of microair vehicles (MAVs) (Truong *et al.*, 2013), where there is an interest in mimicking both the flight and performance of birds and insects. Airfoil flows are also important for developing unmanned aerial vehicles (UAVs) with reduced drag and noise. In this context, a new class of VTOL vehicles including quadcopters and drones is attracting engineers and scientists to design shrouded rotors with more efficient airfoils with enhanced lift characteristics. A decrease of the available area for airports and military bases will also bring the necessity of aircraft with vertical take-off and landing (VTOL) characteristics such as the Bell Boeing V-22, YAK-38 and the Harrier (Barderama *et al.*, 2019; Blackwood and King, 2018; Footohi *et al.*, 2019) all of which are cited with common interests: drag and noise reduction, increased lift, autonomy and energy efficiency.

Most applications of the airfoil flows described above occur at sufficiently high Reynolds numbers for which the boundary layers and wakes are turbulent. In order to understand the characteristics of different airfoils for a range of applications, a study of turbulence properties of such flows is necessary. In this work, we employ high fidelity simulations, in particular, Large Eddy Simulation (LES), of a flow past a NACA0012 airfoil at 5 deg. angle of incidence. Although there are several studies of free shear flows and channels (Pope, 2000) in the literature, applications of wall-resolved LES to airfoils represent a more recent topic of study. Differently from channel flows, airfoils have finite chords and, hence, represent a combination of wall-bounded turbulent flows with free shear flows. The effects of anisotropy found in channel flows are also present in this class of flows but, here, the pressure gradient has a variation. Airfoil flows may also be heavily tripped to mimic wind tunnel experiments, a condition that is not found in channel flows. Such tripping mechanism may introduce different turbulent structures in the flow which have important roles in noise generation and drag.

In the current work, we present a study of turbulence quantities in the flow past a NACA0012 airfoil trying to understand physical phenomena related to tripping and large-scale turbulent structures. LES of airfoil flows may add some non-physical characteristics to the flow such as periodical boundary conditions. Here, we provide an assessment of such features in order to verify the impact of mesh refinement.

## 2. NUMERICAL METHODOLOGY

The present LES calculations solve the compressible Navier Stokes equations in conservative form using general curvilinear coordinates. The spatial discretization of these equations comprises a compact scheme of sixth order accuracy (Nagarajan *et al.*, 2003) implemented in a staggered mesh. Compact finite difference schemes are non-dissipative and, consequently, there is a need for filtering the solution, once numerical instabilities may grow due to non-uniform meshes and other numerical discretization errors. The current filter is applied only at high wavelengths in order to preserve the physics of turbulence (Lele, 1992). In the present simulations, we make use of overset grids with a fourth-order accurate Hermite interpolation between grid blocks (Bhaskaran *et al.*, 2010) in order to better resolve the boundary layers and wakes along the airfoil.

The temporal integration of the equations are carried out by second-order scheme of Beam and Warming (1978) in the near-wall region in order to overcome the time step restriction typical of very fine wall-normal boundary layer grids. Away from solid walls, we advance the solution over time using a third-order Runge-Kutta scheme. In the wall boundaries, the non-slip condition is employed for an adiabatic wall. In the spanwise direction we employ a periodic boundary condition and, in the farfield, boundary conditions are based on characteristic variables (Riemann invariants), besides the application of a buffer layer which dissipates eventual acoustic waves. Different simulations are performed in this work and we assess the effects of a dynamic Smagorinsky (Lilly, 1992) subgrid model on the solutions. In this sense, the SGS model is switched on and off, depending on the simulation and, therefore, the simulations become implicit LES (ILES).

## 3. FLOW AND MESH CONFIGURATIONS

The study and simulation of the NACA0012 airfoil was first performed by Wolf (2011) and results were compared and validated in terms of acoustic quantities against experiments performed by Brooks *et al.* (1989). All simulations studied in this work are run for a flow configuration with Reynolds number based on the airfoil chord  $Re_c = 408.000$  and freestream Mach number  $M_\infty = 0.115$ . The airfoil is set at 5 deg. angle of attack. Different tripping configurations are tested. In order to disturb the boundary layer and mimic the flow configuration from Brooks et al, regions with suction along  $0.15 < x/c < 0.175$  and blowing over the region  $0.175 < x/c < 0.20$  are implemented. The suction and blowing have magnitudes  $U_{blowing} = -U_{suction} = 0.03U_\infty$ , where  $U_\infty$  represents the freestream velocity. Due to tripping and an adverse pressure gradient, the boundary layer becomes turbulent on the suction side of the airfoil. On the pressure side, the boundary layer is always laminar since no tripping is applied in this region and the flow has a favorable pressure gradient. Wolf (2011) employ a three-dimensional tripping in the spanwise direction. However, we also tested a two-dimensional tripping as discussed Ricciardi *et al.* (2019). When the 2D tripping is applied, the SGS subgrid model is switched off while the 3D tripping has the SGS model turned on.

The present mesh configurations consist of body-fitted O-grid blocks designed to accurately resolve the turbulent boundary layer on the suction side of the airfoil. The O-grid blocks have a greater concentration of points (approximately 75%) in the suction side and use a mesh stretching function consisting of a hyperbolic tangent in the normal direction of the airfoil wall. In the background, a Cartesian grid block with uniform resolution around the O-grid block is employed in the overset mesh procedure. Figure 1 shows a comparison of the meshes used in the current investigation. A detail view can be seen including the refinement employed for the two meshes. In Fig. 1 (d), one may notice the vertical divisions in the detail view of the O-mesh. These are due to the mesh writing in CGNS format which facilitate the mesh visualization in zones and the post-processing of data. The figures show every 6 points in order to allow a better visualization of the meshes. Table 1 presents details between the meshes in terms of resolution and tripping configuration.

Table 1. Different meshes and tripping configurations. The values  $n_x, n_y, n_z$  represent the number of points in the  $x, y, z$  coordinates, respectively. The terms  $\Delta x_w^+, \Delta y_w^+$  and  $\Delta z_w^+$  depict the mesh resolution on the first element near the airfoil surface, in viscous units. The subscripts “max” and “TE” represent maximum values computed along the airfoil surface and those near the airfoil trailing edge, along the suction side.

Simulations	$O$ -grid ( $n_x, n_y, n_z$ )	$\Delta x_{w_{max}}^+$	$\Delta y_{w_{max}}^+$	$\Delta z_{w_{max}}^+$	$\Delta x_{w_{TE}}^+$	$\Delta y_{w_{TE}}^+$	$\Delta z_{w_{TE}}^+$	Tripping
(Wolf, 2011)	960 x 125 x 128	63.5	0.63	21	14.5	0.39	13	3D
Current refined mesh	1200 x 190 x 144	50.5	0.58	18	11	0.37	11.5	2D

## 4. RESULTS

The results of the simulation conducted are presented in Fig. 2 in terms of isosurfaces of Q-criterion. It is possible to observe the development of the turbulent boundary layer along the suction side of the airfoil. For this case, the tripping is two-dimensional and some 2D structures form downstream the tripping region. Later, these structures are disturbed transitioning to a fully turbulent flow as can be seen in the detail view of the trailing edge region.

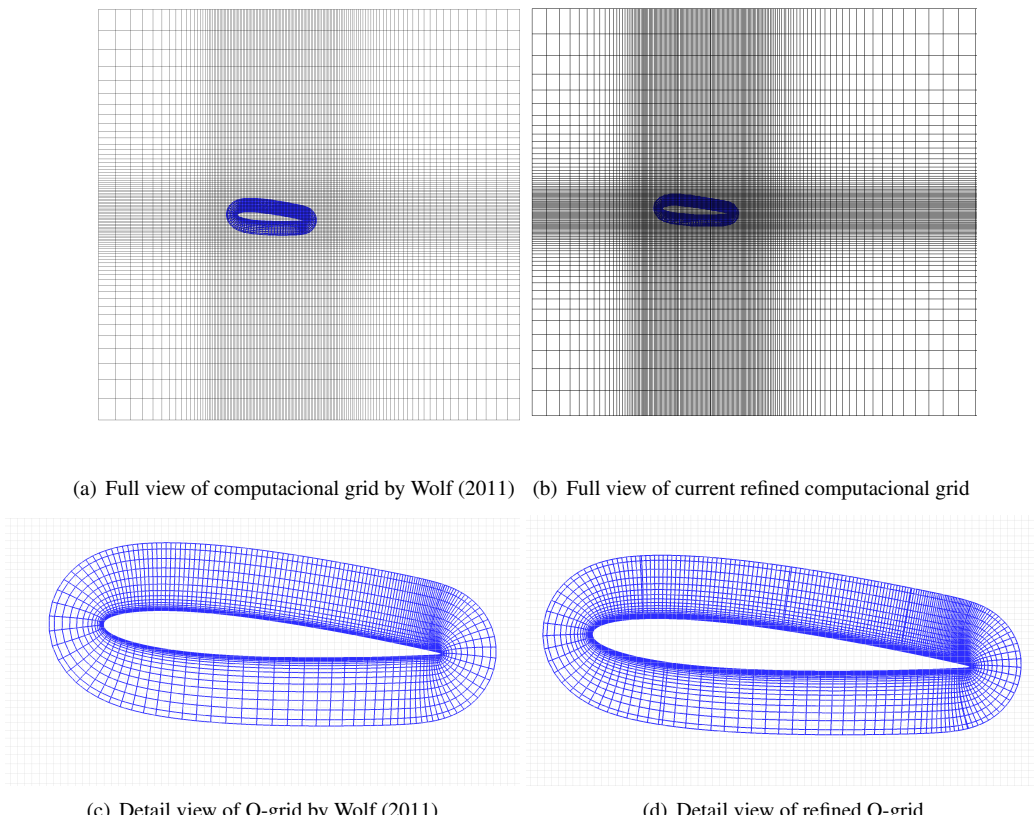


Figure 1. Comparison of different meshes for NACA0012 airfoil (every 6th grid point shown).

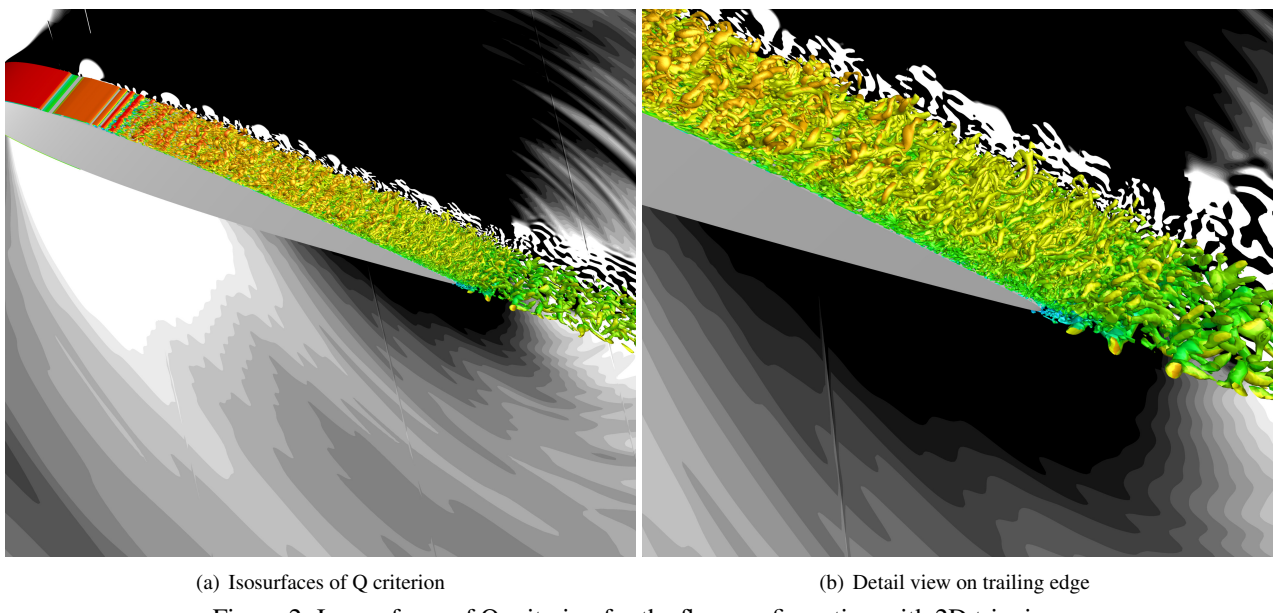
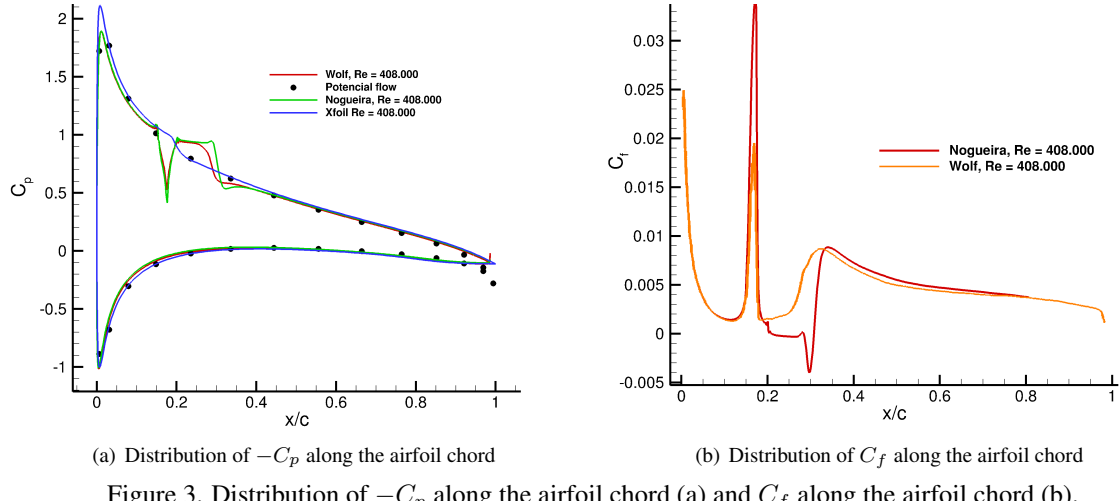
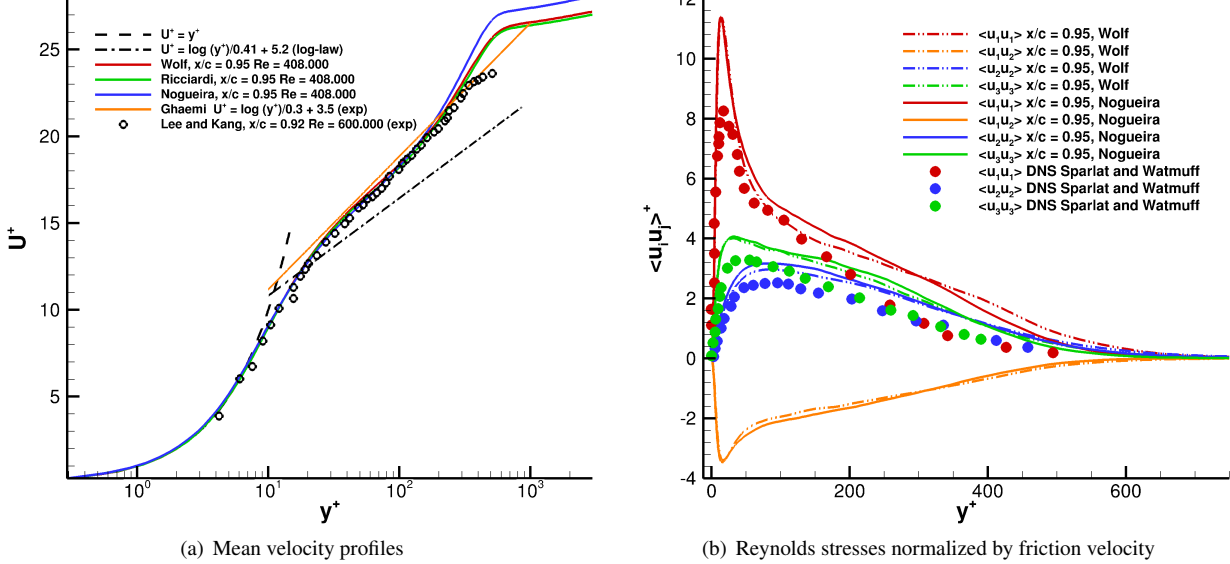


Figure 2. Iso-surfaces of Q criterion for the flow configuration with 2D tripping.

Figure 3 (a) shows the distribution of pressure coefficient  $C_p$  along the airfoil surface for the current refined mesh. This result is then compared to the simulation by Wolf (2011), the Xfoil code (Drela, 1989) and potential flow theory. As can be noticed, there is a good agreement among the current result and other calculations despite the different tripping configurations. Xfoil captures a stronger suction peak at the leading edge but, overall, solutions are similar. The potential flow solution has a small discrepancy at the trailing edge due to its non-viscous nature. Along the tripping regions, both LES calculations have similar results induced by the suction and blowing tripping. Figure 3 (b) shows the surface distribution of friction coefficient defined as  $C_f = \frac{\tau_w}{(1/2\rho U_e)}$ . Here,  $\tau_w$  is the wall shear stress and  $U_e$  is the velocity at the edge of the boundary layer. As can be seen, both LES results present good agreement. However, for the 2D tripping, there

(a) Distribution of  $-C_p$  along the airfoil chord(b) Distribution of  $C_f$  along the airfoil chordFigure 3. Distribution of  $-C_p$  along the airfoil chord (a) and  $C_f$  along the airfoil chord (b).

is a region of negative friction coefficient which indicates the appearance of a small recirculation bubble just downstream the blowing region. The 3D tripping keeps the flow absent from this bubble probably because of longitudinal vortical structures that add momentum to the flow.



(a) Mean velocity profiles

(b) Reynolds stresses normalized by friction velocity

Figure 4. Mean velocity profiles normalized by friction velocity plotted (a) and normalized Reynolds stress (b).

Figure 4 shows the mean velocity profile normalized by friction velocity as function of wall units  $y^+$ . As in Wolf (2011), the log law regions presents a shift in the mean velocity profile when compared to the standard log-law. In the same figure, one can see the mean velocity profiles of Ricciardi *et al.* (2019) obtained with the two-dimensional tripping in the suction side, demonstrating that the tripping configurations does not have a considerable impact on the log region. The velocity profile obtained by the present simulation with a refined mesh is also computed using a two-dimensional tripping. For this case, however, a mesh refinement is employed, which causes a small change in the slope in the log region when compared to the typical von Kármán slope obtained for a flat plate.

Although the mean velocity profiles do not match the typical log-law for flat plates, we show that the current results match some recent experiments performed for NACA0012 airfoils at similar flow conditions (Ghaemi and Scarano, 2011). In addition, similar results are also found by Lee and Kang (2000) for even higher Reynolds numbers,  $Re_c = 600.000$ . Therefore, possible variations of pressure gradient on the airfoil, as well as curvature effects, may shift the velocity profiles for the current airfoil flows compared to the classic flat plate.

Some further flow statistics are shown in Fig. 4(b) through the distribution of Reynolds stresses normalized by friction velocity. Results are also compared to Spalart and Watmuff (1993) for a flat plate under a similar adverse pressure gradient. As one can see, results obtained for the current refined mesh and for the previous one from Wolf (2011) are similar.

In order to investigate the effects of turbulence anisotropy state of the Reynolds Stresses are characterized by trajectory-

ries of the invariant anisotropy tensor in the Lumley triangle (Choi and Lumley, 2001). All possible states of turbulence must be found within the Lumley triangle in invariant coordinates. The normalized Reynolds tensor  $b_{ij}$  is computed as:

$$b_{ij} = \frac{\langle u'_i u'_j \rangle}{\langle u'_k u'_k \rangle} - \frac{\delta_{ij}}{3}. \quad (1)$$

Due to a normalization of the tensor  $b_{ij}$  when turbulence becomes isotropic all fluctuations  $u'_i$  have the same magnitude and the anisotropy tensor goes to zero. Non-zero values represent the degree of anisotropy in each principal direction. The invariants of the second-order tensor are given by I, II, III as:

$$I = b_{ii}, \quad II = -\frac{b_{ij}b_{ji}}{2}, \quad III = \frac{b_{ij}b_{jk}b_{ki}}{3}. \quad (2)$$

In order to verify the behavior of the return isotropy and its respective trajectory, Choi and Lumley (2001), introduced new variables  $\xi$  and  $\eta$  so the turbulence triangle can also be transformed from the II-III coordinates to  $\xi$ - $\eta$  coordinates. In this way, the isotropic behavior is observed in the origin of  $\xi$ - $\eta$  coordinate system. The upper limit of the triangle represents a state of 2-D turbulence, and the left and right sides of the triangle represent axisymmetric turbulence and one dimensional turbulence is found in top corner of the triangle, on the right. The Lumley triangle at different positions along the chord of airfoil is shown in Fig. 5.

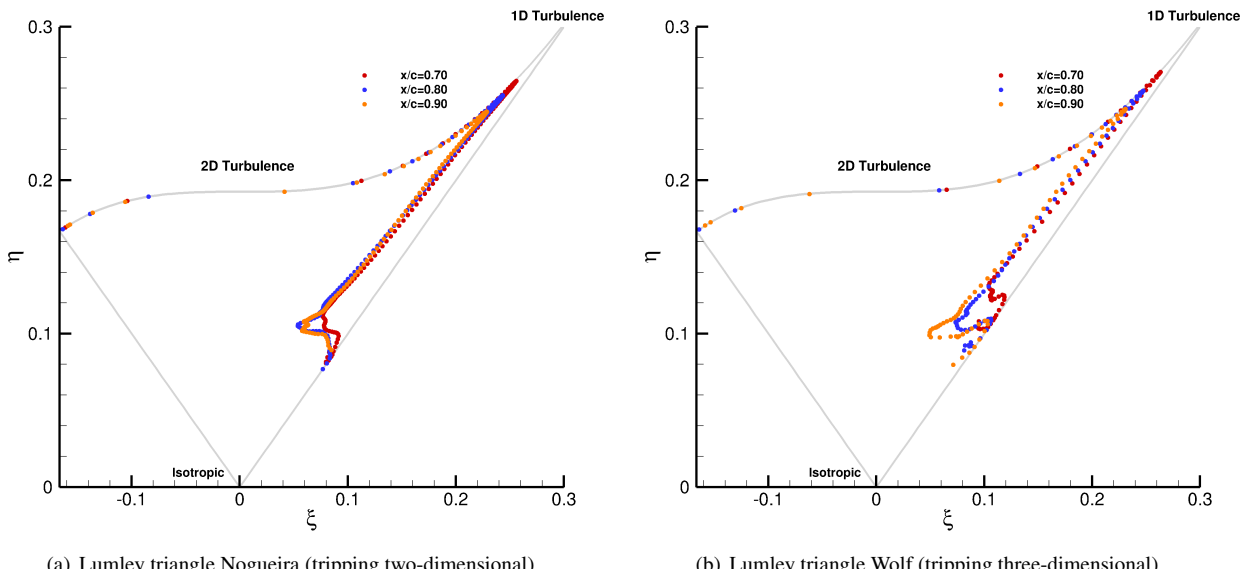
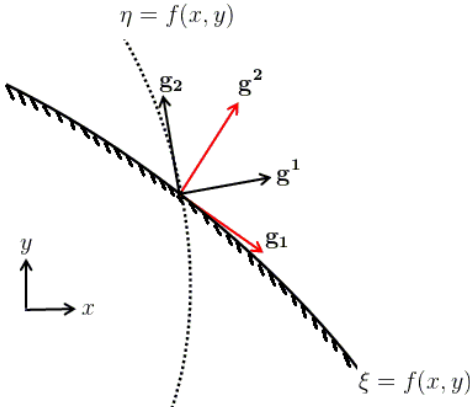


Figure 5. Trajectories along the Lumley triangle for different positions and different tripping configurations of airfoil.

The triangle is computed for different chord positions to the limit of the boundary layer thickness. As can be seen, near the wall the turbulence is two-dimensional and as  $y^+$  increases, the turbulence tends to be one-dimensional mainly due to an increase of the velocity fluctuation  $u'$ . Around  $y^+ \approx 8$  turbulence becomes almost unidimensional and, in this region, on the buffer layer we will find the highest level of production. For  $y^+$  greater than 8 turbulence becomes three-dimensional towards isotropic state. Also, it is interesting to note that turbulence becomes more one-dimensional for positions further upstream along the airfoil chord. In addition, it is possible to notice that when the turbulence becomes closer to the one-dimensional there is a better resolution in Nogueira when compared to Wolf and for log-law regions between the inner layer and outer layer it is possible to note that the three-dimensional tripping by Wolf tends to reach a more isotropic turbulence when compared to Nogueira.

Independently of the orientation of the coordinate system for the Lumley triangle the anisotropy is the same since it is obtained from the invariants of the normalized anisotropy tensor. Subsequently, the normalized anisotropy tensor ( $b_{ij}$ ) was obtained, however, for the tensor  $b_{ij}$  it is necessary to orient the velocity field in the normal and tangential directions so that the flow is aligned with the airfoil. As the mesh has stretching both in the x and y directions, the metric terms are required to compute derivates. The metric terms are taken from the physical plane and modified to a uniform mesh in the computational plane so that  $(x, y) \rightarrow (\xi, \eta)$  (Pulliam and Zingg, 2014).

The tangential and normal velocity components are created from the projection of the velocity vector in the covariant  $g_i$  and contravariant  $g^i$  direction (Hung, 2002) as shown in the Fig. 6.

Figure 6. Contravariant and covariant basis vectors,  $g^i$  and  $g_i$ 

The covariant  $\vec{g}_i$  and contravariant  $\vec{g}^i$  basis vectors are computed as:

$$\vec{g}_1 = \frac{x_\xi \vec{i} + y_\xi \vec{j}}{\sqrt{x_\xi^2 + y_\xi^2}} ; \quad \vec{g}_2 = \frac{x_\eta \vec{i} + y_\eta \vec{j}}{\sqrt{x_\eta^2 + y_\eta^2}} \quad (3)$$

$$\vec{g}^1 = \nabla \xi = \frac{\xi_x \vec{i} + \xi_y \vec{j}}{\sqrt{\xi_x^2 + \xi_y^2}} ; \quad \vec{g}^2 = \nabla \eta = \frac{\eta_x \vec{i} + \eta_y \vec{j}}{\sqrt{\eta_x^2 + \eta_y^2}} . \quad (4)$$

Therefore the velocity vector  $\vec{V} = u \vec{i} + v \vec{j}$  will have its normal  $V_n$  and tangential  $V_t$  components given by:

$$V_t = \vec{V} \cdot \vec{g}_1 = \frac{u x_\xi + v y_\xi}{\sqrt{x_\xi^2 + y_\xi^2}} , \quad (5)$$

$$V_n = \vec{V} \cdot \vec{g}^2 = \frac{u \eta_x + v \eta_y}{\sqrt{\eta_x^2 + \eta_y^2}} . \quad (6)$$

Since the velocity is obtained in terms of the normal and tangential velocities in the direction of airfoil surface, the normalized anisotropy tensor ( $b_{ij}$ ) is obtained in order to verify how the velocity fluctuations vary along the boundary layer, as shown in Fig. 7.

Through the profiles shown for positions  $x/c = 0.7, 0.8$  and  $0.9$  it is possible to identify how the processes evolve along  $y^+$ . Note that near the wall the transversal velocity fluctuation is predominant in relation to the other velocity fluctuations which according to Harun and Lotfy (2018) is highly associated with the physical mechanism of hairpin formation and consequently to the sweep mechanism induced by outward flow and ejection induced by inward flow.

The fluctuation of the normal velocity is practically invariant until reaching the region of  $y^+ \approx 10$ , this locality being the region of highest turbulence production and where the tangential velocity fluctuation component also reaches its maximum value in magnitude. In addition, it is interesting to note that very close to the wall, as it approaches the trailing edge, the velocity fluctuations  $w' w'$  are very close to  $V_t V_t$ , where at  $x/c = 0.8$  it has an equal magnitude. When compared the normalized anisotropy tensor between Wolf and Nogueira both exhibit the same behavior with sensitive changes to  $y^+ > 10^2$  possibly caused by the mesh refinement difference.

Subsequently, turbulent kinetic energy (TKE) balances are computed along the chord to ascertain the effect of adverse pressure gradient on production, dissipation and diffusion of turbulence. The turbulent kinetic energy transport equation can be written as:

$$\frac{\partial k}{\partial t} = A + P + T + D + D_p - \epsilon . \quad (7)$$

This equation indicates the balance of advection, production, turbulent transport, viscous diffusion, pressure diffusion, and pseudo-dissipation for turbulent kinetic energy. For a statistically stationary flow, the time derivative must be zero.

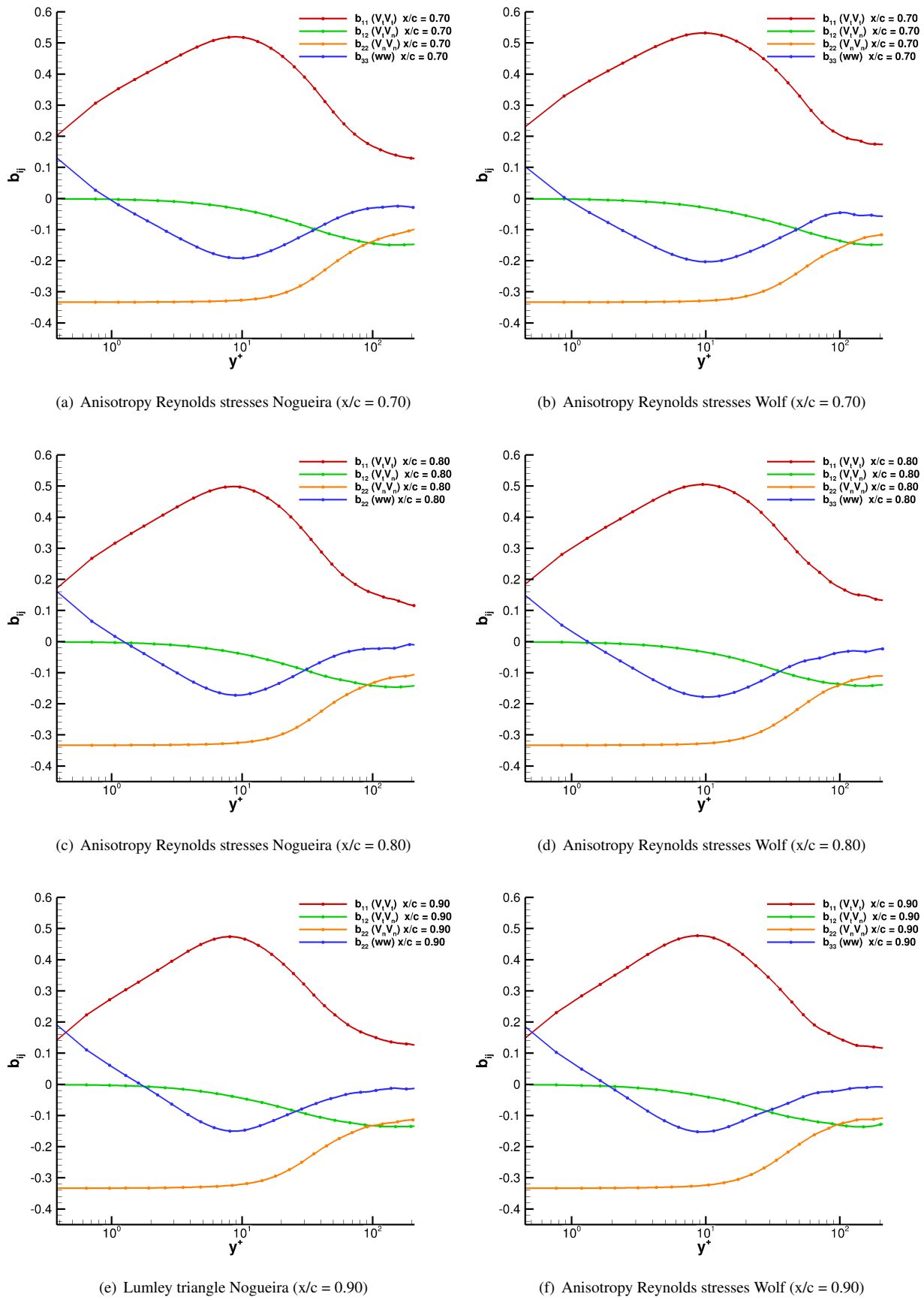


Figure 7. Profiles of anisotropy Reynolds stresses for different positions and different tripping configurations of airfoil.

The terms in the right-hand side of the previous equation are defined as:

$$\text{Advection: } A = -\langle U_j \rangle \frac{\partial k}{\partial x_j}, \quad (8)$$

$$\text{Production: } P = -\left\langle u'_i u'_j \right\rangle \frac{\langle \partial U_i \rangle}{\partial x_j}, \quad (9)$$

$$\text{Turbulent transport: } T = -\frac{1}{2} \frac{\partial \left\langle u'_i u'_i u'_j \right\rangle}{\partial x_j}, \quad (10)$$

$$\text{Viscous diffusion: } D = \nu \frac{\partial^2 k}{\partial x_j^2}, \quad (11)$$

$$\text{Pressure diffusion: } D_p = -\frac{1}{\rho} \frac{\partial \left\langle u_i p' \right\rangle}{\partial x_i}, \quad (12)$$

$$\text{Pseudo-dissipation: } \epsilon = -\nu \left\langle \frac{\partial u_i}{\partial x_j} \frac{\partial u_i}{\partial x_j} \right\rangle. \quad (13)$$

All derivatives are calculated using a 10th order compact scheme along with the respective metric terms for the derivatives along the x and y directions. Firstly, the turbulent kinetic energy transport equation was implemented for a channel with the data from a DNS from Moser for validation (Moser *et al.*, 1999) presenting an excellent agreement with the literature. Subsequently, the balance for the airfoil is implemented and unlike the channel that has the homogeneous x and z directions, in the airfoil, there is only the z direction (span). Although there is a lack of data in literature about turbulent boundary layers over airfoils, the TKE of NACA0012 was compared with that from LES of NACA4412 from Henningson *et al.* (2017) showing good behavior. Results are shown for different positions of the airfoil in Fig. 8.

Turbulent kinetic energy budget curves are made non-dimensional by a factor of  $\frac{u_\tau^4}{\nu}$  (Pope, 2000). It is first noticed that very close to the wall the kinetic energy balance is zero. In addition, as the position along the chord is increased towards the trailing edge of the airfoil, the levels of viscous diffusion, production and dissipation increase. Note also that for  $y^+ \approx 10$  there is the highest level of turbulence production. At  $y^+ \approx 20$  there is the largest value in the total kinetic energy balance. Hence, we can see the difference of such solution compared to DNS. This difference is attributed to the filtered scales in the LES and which are not present in pseudo-dissipation term. The behavior of the TKE for both Wolf and Nogueira are very similar, with a significant increase mainly in the terms of the Turbulent Diffusion and Viscous Diffusion in Wolf. In the region at  $y^+ \approx 20$  where the total balance reaches its maximum, Nogueira there is a reduction of about 10% in relation to Wolf.

## 5. CONCLUSIONS

In the current work we employ wall-resolved large eddy simulations to study turbulent flows over a NACA 0012 airfoil. Statistics of the turbulent flows are analyzed in terms of TKE budgets, the Reynolds stress anisotropy tensor and the Lumley triangle. We also show comparisons in terms of pressure and friction coefficients, as well as mean velocity and Reynolds stress profiles. Results show a good agreement between the two meshes considered in the study demonstrating good convergence of results. Comparisons to experimental data also show good agreement in terms of normalized mean flow profiles. We observe in the Lumley triangle that the return to isotropy is slightly different than that typically found for plane channel flows. Statistics obtained by the 2D and 3D tripping are similar for the current analyses despite that, for the former tripping configuration, a small separation bubble is observed just downstream of the tripping location. On the other hand, for the 3D tripping, the flow is fully attached, probably because of longitudinal vortices from the tripping that add streamwise momentum to the flow. We also show that, as the flow reaches the trailing edge, all mechanisms involved in the TKE budget become more pronounced.

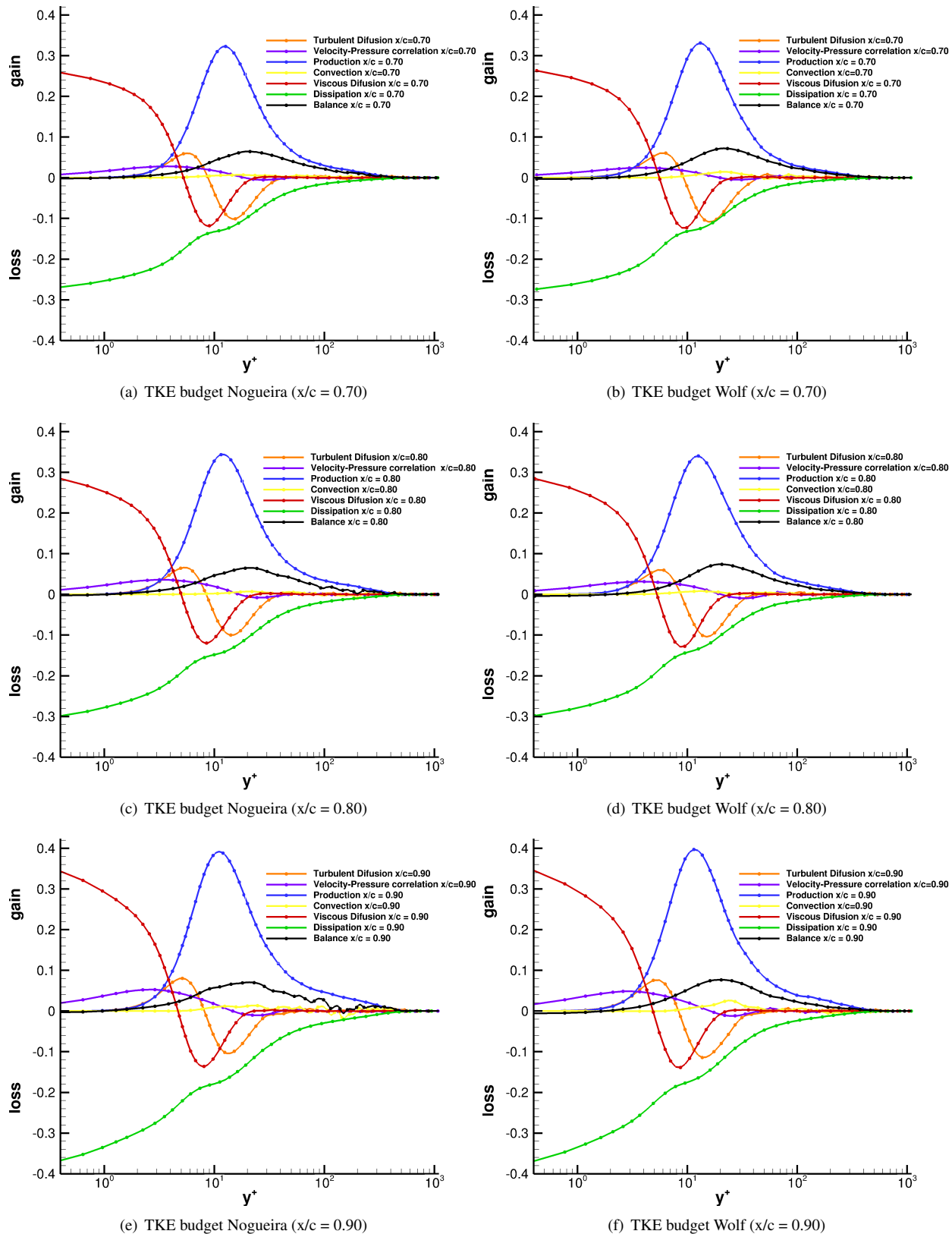


Figure 8. TKE budget for different positions and different tripping configurations of airfoil.

## 6. REFERENCES

- Bardera-Mora, R., Garcia, A.M., Sevillano, A.R. and Montejan, M.B., 2019. "Aerodynamic flow effects on aircraft carrier takeoff performance". *Journal of Aircraft*, Vol. 56, pp. 1005–1013.  
 Beam, R. and Warming, R., 1978. "An implicit factored scheme for the compressible navier-stokes equations". *AIAA*

- Journal*, Vol. 16, pp. 393–402.
- Bhaskaran, R. and S.K., L., 2010. “Large eddy simulation of free-stream turbulence effects on heat transfer to a high pressure turbine cascade”. *Journal of Turbulence*,, Vol. 11, No. 1, pp. 1–15.
- Blackwood, Z. and King, G.S., 2018. “Vertical take-off unmanned aerial vehicle with forward flight”. *The West Indian Journal of Engineering*, Vol. 40, pp. 62–71.
- Brooks, T.F., Pope, D.S. and Marcolini, M.A., 1989. “Airfoil self-noise and prediction”. *Tech. rep., NASA Reference Publication*, Vol. 1218.
- Choi, K. and Lumley, J.L., 2001. “The return to isotropy of homogeneous turbulence”. *Journal of Fluid Mechanics*, Vol. 436, p. 59–84.
- Drela, M., 1989. “XFOIL: An analysis and design system for low reynolds number airfoils”. *Conference Notre Dame, Indiana, USA*, Vol. 54.
- Footohi, P., Bouskela, A. and Shkarayev, S., 2019. “Aerodynamic design of long-range VTOL-UAV”. *AIAA Scitech 2019 Forum*.
- Ghaemi, S. and Scarano, F., 2011. “Counter-hairpin vortices in the turbulent wake of a sharp trailing edge”. *Journal of Fluid Mechanics*, Vol. 689, p. 317–356.
- Gourdain, N., Singh, D., Jardin, T. and S.Prothin, 2017. “Analysis of the turbulent wake generated by a micro air vehicle hovering near the ground with a lattice boltzmann method”. *Journal of the american helicopter society*, Vol. 62, pp. 1–12.
- Harun, Z. and Lotfy, E.R., 2018. *Generation, Evolution, and Characterization of Turbulence Coherent Structures*. IntechOpen, London,United Kingdom, 1st edition.
- Henningson, D.S., Philipp, S., Hanifi, A., Negi, P. and Vinuesa, R., 2017. “Unsteady aerodynamic effects in pitching airfoils studied through large-eddy simulations”. *10th Internacional Symposium on Turbulence and Shear Flow Phenomena*.
- Hung, C., 2002. “Definition of contravariant velocity components”. *Tech. rep., NASA Reference Publication (NASA Ames Research Center)*.
- Lee, H. and Kang, S.H., 2000. “Flow characteristics of transitional boundary layers on an aerofoil in wakes.” *ASME: Journal of Fluids Engineering*, Vol. 122, pp. 522–532.
- Lele, S., 1992. “Compact finite difference schemes with spectral-like resolution”. *Journal of Computational Physics*,, Vol. 103, pp. 16–42.
- Li, Y., Castro, A., Sinokrot, T. and Carrica, W.P.P., 2015. “Coupled multi-body dynamics and cfd for wind turbine simulation including explicit wind turbulence”. *Elsevier*, Vol. 76, pp. 338–361.
- Lilly, D.K., 1992. “A proposed modification of the germano subgridscale closure method”. *Physics of Fluids A: Fluid Dynamics*, Vol. 4, pp. 633–635.
- Moser, R.D., Kim, J. and Mansour, N.N., 1999. “Direct numerical simulation of turbulent channel flow up to  $re = 590$ ”. *Physics of Fluids*, Vol. 11, pp. 943–945.
- Nagarajan, Lele, S., S.K. and Ferziger, J., 2003. “A robust high-order method for large eddy simulation”. *Journal of Computational Physics*,, Vol. 191, p. 392–419.
- Oerlemans, S., 2009. *Detection of aeroacoustic sound sources on aircraft and wind turbines*. Ph.D. thesis, University of Twente.
- Pope, S.B., 2000. *Turbulent Flows*. Cambridge University Press, New York, 1st edition.
- Pulliam, T. and Zingg, D., 2014. *Fundamental Algorithms in Computational Fluid Dynamics*. Springer, New York, 1st edition.
- Ricciardi, T.R., Ribeiro, J.H.M. and Wolf, W.R., 2019. “Analysis of coherent structures in large-eddy simulations of a NACA0012 airfoil”. *AIAA Scitech 2019 Forum*.
- Spalart, P.R. and Watmuff, J.H., 1993. “Experimental and numerical study of a turbulent boundary layer with pressure gradient”. *Journal of Fluid Mechanics*, Vol. 249, pp. 337–371.
- Truong, T.V., Byun, D., Kim, M.J., Yoon, K. and C.Park, H., 2013. “Aerodynamic forces and flow structures of the leading edge vortex on a flapping wing considering ground effect”. *IOP Science Journals*, Vol. 8.
- Wolf, W.R., 2011. *Airfoil aeroacoustics: LES and acoustic analogy predictions*. Ph.D. thesis, Stanford University.

## 7. RESPONSIBILITY NOTICE

The authors are the only responsible for the printed material included in this paper.